Nanomechanical mechanism for lipid bilayer damage induced by carbon nanotubes confined in intracellular vesicles

Wenpeng Zhu[a,b,1], Annette von dem Bussche[c,1,2], Xin Yi[a,1], Yang Qiu[a], Zhongying Wang[a], Paula Weston[c], Robert H. Hurt[a,d], Agnes B. Kane[c,d], and Huajian Gao[a,d,2]

[a]School of Engineering, Brown University, Providence, RI 02912; [b]Department of Engineering Mechanics, Center for Advanced Mechanics and Materials, Key Laboratory of Applied Mechanics, Tsinghua University, Beijing 100084, China; [c]Department of Pathology and Laboratory Medicine, Brown University, Providence, RI 02912; and [d]Institute for Molecular and Nanoscale Innovation, Brown University, Providence, RI 02912

Edited by Howard A. Stone, Princeton University, Princeton, NJ, and approved September 20, 2016 (received for review March 29, 2016)

Understanding the behavior of low-dimensional nanomaterials confined in intracellular vesicles has been limited by the resolution of bioimaging techniques and the complex nature of the problem. Recent studies report that long, stiff carbon nanotubes are more cytotoxic than flexible varieties, but the mechanistic link between stiffness and cytotoxicity is not understood. Here we combine analytical modeling, molecular dynamics simulations, and in vitro intracellular imaging methods to reveal 1D carbon nanotube behavior within intracellular vesicles. We show that stiff nanotubes beyond a critical length are compressed by lysosomal membranes causing persistent tip contact with the inner membrane leaflet, leading to lipid extraction, lysosomal permeabilization, release of cathepsin B (a lysosomal protease) into the cytoplasm, and cell death. The precise material parameters needed to activate this unique mechanical pathway of nanomaterials interaction with intracellular vesicles were identified through coupled modeling, simulation, and experimental studies on carbon nanomaterials with wide variation in size, shape, and stiffness, leading to a generalized classification diagram for 1D nanocarbons that distinguishes pathogenic from biocompatible varieties based on a nanomechanical buckling criterion. For a wide variety of other 1D material classes (metal, oxide, polymer), this generalized classification diagram shows a critical threshold in length/width space that represents a transition from biologically soft to stiff, and thus identifies the important subset of all 1D materials with the potential to induce lysosomal permeability by the nanomechanical mechanism under investigation.

one-dimensional nanomaterials | molecular dynamics | lysosomal permeabilization | biomembrane | lipid extraction

The interactions of low-dimensional materials with the external or plasma membrane of living cells have been the subject of prior studies due to their importance in uptake and delivery, antibacterial action, and nanomaterial safety (1–6). Following uptake, nanomaterials may also interact with internal membranes while under confinement in intracellular vesicles (7–10), but the biophysics of these geometrically constrained systems is poorly understood. Low-dimensional materials interact with biological systems in complex ways dictated by their 1D nanofibrous or 2D nanosheet geometries (7, 11–20). These interactions typically begin when materials encounter the plasma membrane and initiate phenomena that can include adhesion, membrane deformation, penetration, lipid extraction, entry, frustrated uptake, or cytotoxicity (4, 11–14, 19–21). Recent experimental data suggest that the cellular response to some 1D materials is governed by their interaction with the internal lipid-bilayer membranes of endosomes and lysosomes following nanomaterial uptake (7–10). The resulting geometry is fundamentally different in that the fibrous materials are confined within a vesicle, imposing geometric constraints and introducing mechanical forces that act bidirectionally—i.e., on both the thin fibrous structure and the inner leaflet of the soft membrane. The fundamental biophysics of this tube-in-vesicle system is virtually unexplored, yet may be critical for understanding the cellular response to nanotubes/fibers, where shape and stiffness are among the known determinants of toxicity (13, 21). The technique of coarse-grained molecular dynamics (MD), demonstrated to be effective in the study of complex biomolecular systems (22, 23), has been applied to whole lipid-bilayer patches to reveal a biophysical mechanism for carbon nanotube interaction with the plasma membranes leading to tip entry and uptake (4, 19, 20). The same technique may also provide insight relevant to internal membrane interactions, although whole vesicle MD is a significant challenge. Here we use a complement of techniques including coarse-grained MD, all-atom MD, in vitro bioimaging, and carbon nanotube length modification to reveal the behavior of vesicle-encapsulated carbon nanotubes and identify the conditions and carbon nanotube (CNT) types that lead to mechanical stress and membrane damage following cellular uptake and packaging in lysosomes (8).

CNTs Confined in Vesicles: Nanomechanics and Coarse-Grained Molecular Dynamics

We began by exploring the basic nanomechanics of CNTs confined in lipid-bilayer vesicles, focusing on possible physical and

Significance

Recent experimental studies report correlations between carbon nanotube toxicity and tube length and stiffness. Very little is known, however, about the actual behavior of these fibrous nanomaterials inside living cells following uptake, and the fundamental mechanistic link between stiffness and toxicity is unclear. Here we reveal a nanomechanical mechanism by which sufficiently long and stiff carbon nanotubes damage lysosomes, a class of membrane-enclosed organelles found inside cells that are responsible for breaking down diverse biomolecules and debris. The precise material parameters needed to activate this unique mechanical toxicity pathway are identified through coupled theoretical modeling, molecular dynamics simulations, and experimental studies, leading to a predictive pathogenicity classification diagram that distinguishes toxic from biocompatible nanomaterials based on their geometry and stiffness.

Author contributions: W.Z., A.v.d.B., X.Y., R.H.H., A.B.K., and H.G. designed research; W.Z., A.v.d.B., X.Y., Y.Q., and Z.W. performed research; P.W. contributed new reagents/analytic tools; W.Z., A.v.d.B., X.Y., R.H.H., A.B.K., and H.G. analyzed data; and W.Z., A.v.d.B., X.Y., Y.Q., Z.W., R.H.H., A.B.K., and H.G. wrote the paper.

The authors declare no conflict of interest.

This article is a PNAS Direct Submission.

Freely available online through the PNAS open access option.

[1]W.Z., A.v.d.B., and X.Y. contributed equally to this work.

[2]To whom correspondence may be addressed. Email: Annette_von_dem_Bussche@brown.edu or Huajian_Gao@brown.edu.

This article contains supporting information online at www.pnas.org/lookup/suppl/doi:10.1073/pnas.1605030113/-/DCSupplemental.

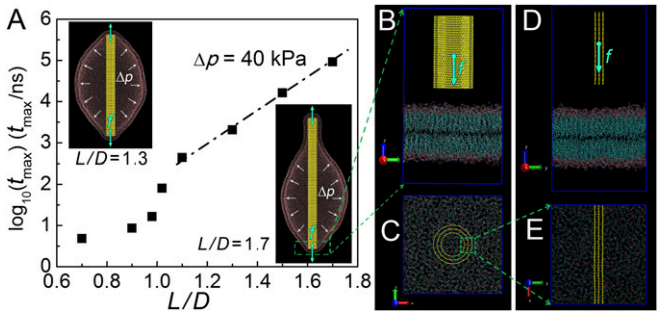

Fig. 1. CGMD simulations of lysosomal membrane disruption induced by encapsulation of a stiff CNT. (*A*) The maximum noninterrupted contact time between an MWCNT and a lysosome (with a diameter D of 100 nm) at different length ratios of L/D and $\Delta P = 40$ kPa. (*Insets*) Equilibrium configurations of the lysosome at $L/D = 1.3$ and 1.7. (*B–E*) Conformations of all-atom simulations in front (*B* and *D*) and top (*C* and *E*) views. (*B* and *C*) A CNT interacting with a membrane. (*D* and *E*) An MLG interacting with a membrane, representing a slice of the near-tip region of the CNT.

mechanical mechanisms of membrane damage and permeabilization. One potential damage mechanism is mechanical burst, as membrane tension increases in response to lysosomal enlargement forced by encapsulation of long, stiff tubes. We performed a theoretical analysis of a rigid CNT of length L trapped in the interior of a lysosome with typical diameter $D = 1$ μm, osmostic pressure $\Delta p = 300$ Pa, and membrane bending stiffness $\kappa = 20\ k_BT$ ($1\ k_BT = 4.2$ pN · nm) (*SI Appendix*, Figs. S1 and S2). A sufficiently long nanotube causes the formation of a membrane tether, and the lysosome exerts a compressive force around $f = 20$ pN on the nanotube (*SI Appendix*, Fig. S2*A*). Depending on the nanotube length, the maximum membrane tension can reach $\sigma = 0.08$ mN/m (*SI Appendix*, Fig. S2*B*), which is still much lower than the experimental value of 4–10 mN/m required for instantaneous vesicle lysis (24). These results suggest that lysosomal rupture through CNT-induced membrane tension is unlikely to be the major mechanism of membrane permeabilization.

We then pursued the alternative hypothesis that nanotube confinement leads to local membrane damage due to sustained, direct, forced contact between multiwalled CNT (MWCNT) tips and the inner membrane leaflet. To assess this hypothesis, coarse-grained MD (CGMD) simulations were performed to investigate the maximum noninterrupted contact time t_{max} between a confined tube and the lysosomal membrane at the nontether end (Fig. 1*A* and *SI Appendix*, section 5 and Fig. S6). Our theoretical relations $\sigma D^2/\kappa = F_1(\Delta pD^3/\kappa, L/D)$ and $fD/\kappa = F_2(\Delta pD^3/\kappa, L/D)$ suggest that two dimensionless parameters $\Delta pD^3/\kappa$ and L/D govern the problem under consideration (*SI Appendix*, section 1). Guided by this insight, we were able to substantially reduce computational costs by considering a lysosome with diameter of 100 nm under an osmotic pressure of 40 kPa, which would have dimensionless parameters $\Delta pD^3/\kappa$ and L/D very similar to those of typical lysosomes with diameter from 0.1 to 1.2 μm (25) under osmotic pressure of 300 Pa (*SI Appendix*, section 4). A sufficiently long MWCNT leads to a cherry-shaped structure with one end of the nanotube encapsulated in a membrane tether and the other nontethered end directly indenting the lipid bilayer (Fig. 1*A*, *Insets*). Similar structures have been observed in our theoretical calculations (*SI Appendix*, Fig. S1) and extraction of membrane tubes by optical tweezers (26). Note that this asymmetric configuration has lower energy than the symmetric configuration tethered at both ends (*SI Appendix*, Figs. S3*D* and S4). If the tube length L is smaller than the lysosome diameter D, thermal fluctuations tend to prevent sustained contact. However, if the encapsulated tube is long and stiff, fluctuation is limited by confinement and long-term noninterrupted contact becomes possible. Fig. 1*A* shows that larger L/D values lead to longer maximum noninterrupted contact time t_{max}, which increases exponentially with L/D in the range $L/D > 1$, regardless of the membrane composition and tube diameter (*SI Appendix*, section 7 and Figs. S8–S10). This exponential dependence is consistent with the prediction by Bell's model extending the classical rate theory for chemical reactions to account for the effect of an external force (27) (*SI Appendix*, section 1). By extrapolating the simulation results to experimental timescales, the maximum noninterrupted contact time goes up to 1 h as L/D reaches 3.62 (*SI Appendix*, section 6 and Fig. S7). Therefore, the length of an encapsulated nanotube, despite having minor influence on membrane tension and compressive force, plays a critical role in determining the maximum noninterrupted contact time between the nanotube and inner membrane leaflet. Understanding the consequences of this prolonged local contact requires all-atom MD simulations.

All-Atom MD Shows Phospholipid Extraction by Long MWCNTs

We used all-atom MD methods to assess our hypothesis that local lysosomal membrane damage is caused by the above-predicted mechanical contact between a nanotube tip and the inner membrane leaflet. To limit the size of the simulation, we considered a multilayered graphene (MLG) sheet as a model for a cross-sectional slice of the end section of an MWCNT interacting with a lipid bilayer (Fig. 1 *B–E* and *SI Appendix*, section 8). This local view allowed us to focus on the effect of a vertical graphenic surface near the tip of a nanotube on the lipid bilayer. A constant force F_c was applied to mimic the compressive force on the nanotube associated with confinement. To expedite the local membrane damage within the timescale of all-atom simulations, a larger compressive force is assumed in simulating the critical damage time, which is then extrapolated to the time- and force scales in the experiments. Fig. 2 *A–D* shows representative configurations of a three-layer graphene sheet interacting with a dipalmitoyl phosphatidylcholine (DPPC) lipid bilayer under a compressive force of 500 pN. At the onset of contact, the membrane was able to endure the compressive force

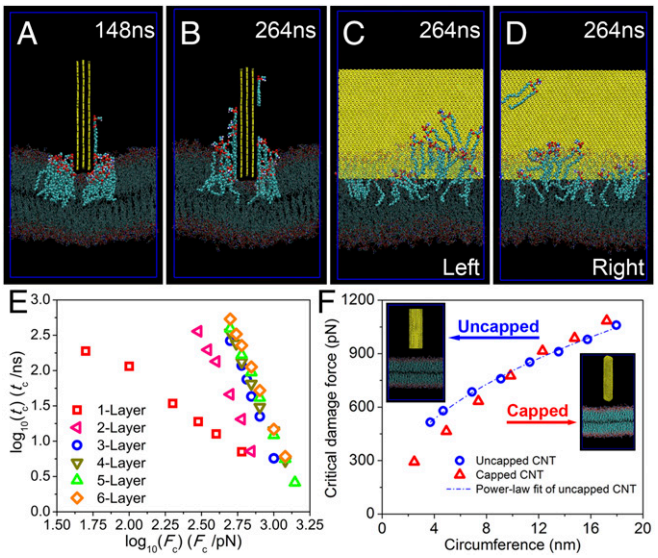

Fig. 2. All-atom MD reveals a nanomechanical mechanism of lipid extraction caused by enforced mechanical contact for lysosomal permeabilization. (*A–D*) Representative configurations of a three-layer graphene sheet interacting with a DPPC membrane under a compressive force of 500 pN at 148 ns (*A*) and 264 ns (*B–D*). (*C* and *D*) Left and right views of *B*, respectively. MLG sheets are shown in yellow. Phospholipids are shown as chains of atoms colored to identify hydrophilic and hydrophobic regions (hydrogen, white; oxygen, red; nitrogen, dark blue; carbon, cyan; phosphorus, orange). Extracted phospholipids are highlighted as chains of larger spheres. Water molecules are set to be transparent for clarity. (*E*) The critical damage time leading to lysosomal permeability as a function of the contact force induced by the MLG. (*F*) The dependence of critical damage forces on the circumference of uncapped and capped CNTs.

from the vertical graphene surface without disruption, but lipid extraction by graphenic surface that is energetically favorable (*SI Appendix*, section 15 and Fig. S15) was observed in the snapshot at 148 ns. The early lipid extraction events were slow and steady despite some loss of membrane integrity. However, at 264 ns, the lipid extraction process suddenly became faster and disruptive with clusters of lipids climbing the vertical graphene surface. The instability of lipid extraction results in a permeable membrane that would allow leakage of lysosomal contents into the cytoplasm. The critical damage time t_c for the membrane to become permeable is defined as the onset of the burst of lipid extraction, corresponding to the inflection points in the curves of center-of-mass distances in *SI Appendix*, section 10, Fig. S11. Similar lipid extraction was shown by Tu et al. in modeling the interaction between graphene nanosheets and bacterial membranes in the absence of a compressive force (1). Note that the interaction between finite-sized graphene nanosheets and lipid bilayers could be strongly facilitated by the corners of the nanosheets (2). In our present simulations, the MLGs represent a slice of an MWCNT and hence have no corners. In this case, as spontaneous lipid extraction is hindered by a high energy barrier (2), a compressive force on the nanotube is required and its magnitude can be correlated to the critical damage time t_c. Fig. 2*E* shows that the critical condition to induce lysosomal permeabilization can be expressed as a power-law relationship between the contact force and the critical damage time, with lower contact force postponing membrane damage, which is insensitive to membrane composition (*SI Appendix*, section 14 and Fig. S14). Interestingly, t_c only has a weak dependence on the number of graphene layers (Fig. 2*E*), corresponding to the number of nanotube walls. Further investigation revealed that this weak dependence is due to the localization of contact force distribution at the inner and outer layers of the MLG (*SI Appendix*, section 11 and Fig. S12). Note that similar lipid extraction processes have been observed on a small MWCNT (*SI Appendix*, Fig. S16*A*) and on an MLG–membrane system of smaller lateral size (*SI Appendix*, Fig. S16 *B* and *C*). The geometrical effects of the nanotube tip are shown in Fig. 2*F*, which enables us to calculate t_c by an MWCNT (see details in *SI Appendix*, sections 12 and 13 and Fig. S13).

Combining the results of CGMD and all-atom simulations allows a prediction of the link between material properties and lysosomal damage. The CGMD simulations show that the maximum noninterrupted contact time between the nanotube and lysosome increases exponentially with the tube length. When the maximum noninterrupted contact time exceeds the critical damage time, membrane permeability is induced through the lipid extraction instability observed in our all-atom simulations. It can thus be predicted that, at the same radius, longer nanotubes induce longer contact time and thus lysosomal membrane permeabilization leading to cell toxicity, in agreement with our experimental results described next.

Model Validation—Imaging of Nanotube Uptake and Vesicle Interactions

A variety of bioimaging modalities were used to test the nanomechanical model predictions and reveal their implications for cell response and toxicity. A panel of carbon nanomaterials of widely varying geometry was created by a combination of acquisition, oxidative shortening, and detailed characterization of the as-received and processed materials (*SI Appendix*, Table S3 and Figs. S19–S22). From that panel, one long, stiff nanotube sample (MWCNT-7) and a zero-dimensional isometric particle reference sample (carbon black) were delivered to hepatocytes (Fig. 3 and *SI Appendix*, Fig. S26) or lung epithelial cells (*SI Appendix*, Figs. S23 and S24) in culture. Important target cells for CNT toxicity include lung epithelial cells and hepatocytes, and these parenchymal cells are known to internalize nanoparticles by active cellular uptake via endocytosis (28, 29) (Fig. 3 *A* and *B*). Spherical carbon black nanoparticles colocalize with punctate red fluorescent vesicles, indicating intact vesicle membranes (Fig. 3*C* and *SI Appendix*, Fig. S23*C*), and

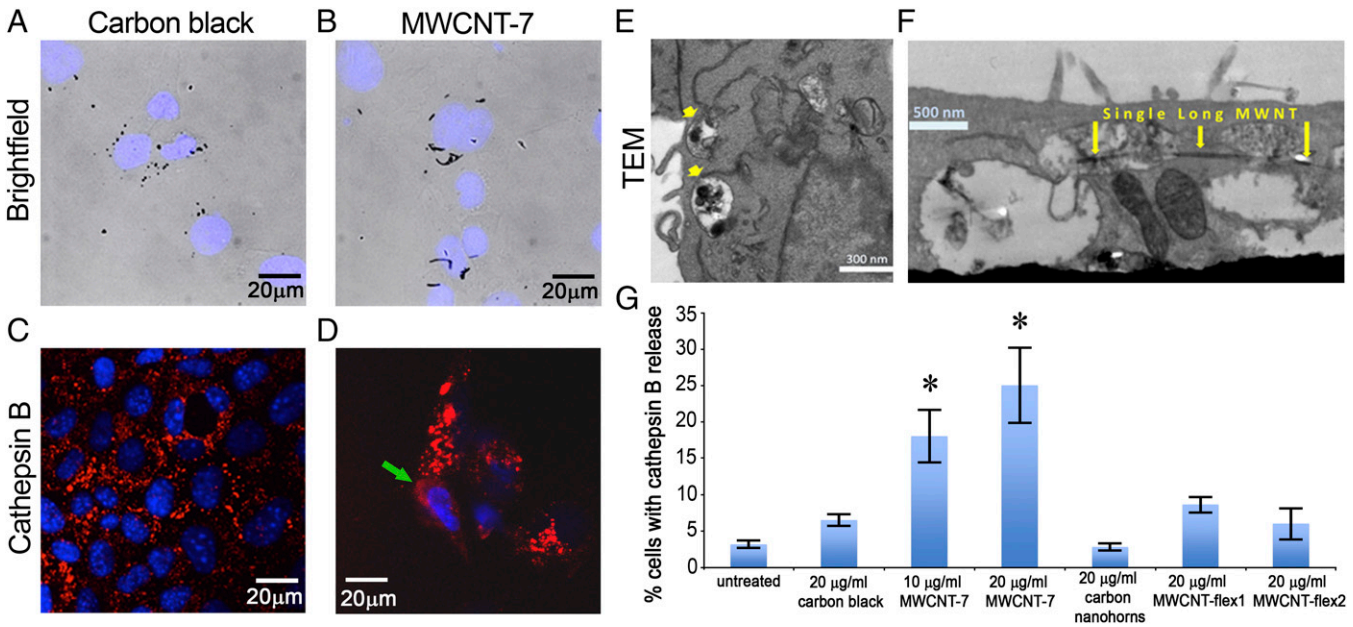

Fig. 3. Cellular uptake, localization, and lysosomal interactions of long, rigid MWCNT-7 and spherical carbon black nanoparticles. (*A* and *B*) Fluorescent microscope images of hepatocytes after 24-h exposure to carbon black or MWCNT-7 combined with bright-field imaging to visualize the particles within the cells and DAPI to visualize the nucleus (blue fluorescence). (*C* and *D*) Lysosomal membrane permeabilization assessed using cathepsin B assay. Green arrow shows example of diffuse fluorescence indicating cathepsin B leakage following nanotube exposure. (*E* and *F*) Intracellular localization of nanomaterials in hepatocytes after 24 h as visualized by TEM. Carbon black colocalizes with lysosomes (yellow arrows), whereas long, rigid MWCNT-7 only partially colocalize with lysosomes. Doses are 10 μg/mL for TEM studies and 20 μg/mL for cathepsin B assay. (*G*) Quantification of diffuse cathepsin B release into the cytoplasm of hepatocytes after exposure to carbon nanomaterials. Diffuse cathepsin B fluorescence was determined using single-cell quantitative high content imaging (Opera Phenix). After exposure of hepatocytes to MWCNT-7, flexible MWCNTs (MWCNT-flex1 and MWCNT-flex2), carbon black and carbon nanohorns for 24 h, only MWCNT-7 induced a significant, dose-dependent release of cathepsin B into the cytoplasm. $*P < 0.05$.

nanoparticle localization in membrane-bound cytoplasmic vesicles was confirmed using transmission electron microscopy (TEM) (Fig. 3*E* and *SI Appendix*, Fig. S30). The MWCNTs were partially colocalized with punctate cytoplasmic vesicles, and longer CNTs were seen penetrating through the vesicle membrane into the cytoplasm by TEM (Fig. 3*F*). Immunogold labeling confirmed that these membrane-bound vesicles are lysosomes (*SI Appendix*, Fig. S30). Lysosomal membrane permeabilization was assessed using a fluorescence assay for a lysosomal protease, cathepsin B, which retains activity following release into the cytoplasm (30). Confocal fluorescence imaging revealed that exposure to CNTs induced low-intensity, diffuse fluorescence reflecting focal release of cathepsin B into the cytoplasm (Fig. 3*D*). Image analysis was used to further distinguish intact lysosomes from permeable ones based on object identification and sizing. Intact lysosomes show narrow size distribution and distinct edges (*SI Appendix*, Fig. S31*A*; high threshold in *SI Appendix*, Fig. S31*B*), whereas permeable lysosomes show weaker, diffuse fluorescence over larger areas in the cytoplasm [*SI Appendix*, Fig. S31*B* (*Right*) and low threshold size distributions] associated with cathepsin B leakage following MWCNT-7 exposure. Additional verification of cathepsin B release and lysosomal damage due to long, stiff MWCNT-7 was obtained using confocal fluorescence microscopy and quantitative high content imaging (Fig. 3*G*). The release of cathepsin B initiates a proteolytic cascade culminating in activation of caspases leading to cell death by apoptosis (31) (shown in Fig. 4*A* and *SI Appendix*, Figs. S28*A*, S24 *C–E*, and S27 *C*, *E*, and *F*). Colocalization of cathepsin B release and caspase activation was demonstrated in lung epithelial cells 24 h after exposure to MWCNT-7 (*SI Appendix*, Fig. S24*E*), suggesting a link between lysosomal damage induced by exposure to long, rigid MWCNT-7 and cell death. The causal link between cathepsin B release and cell toxicity was assessed using a selective cathepsin B inhibitor, methyl ester CA-074. Coexposure of hepatocytes to long, rigid MWCNT-7 and the cathepsin B inhibitor methyl ester CA-074 partially prevented cell death as well as caspase activation (*SI Appendix*, Fig. S18 *B* and *C*). These observations confirm the basic molecular dynamics predictions (*vide supra*) that rigid MWCNTs disrupt lysosomal membrane integrity in a length-dependent manner.

Cellular Response to Carbon Nanomaterials of Diverse Geometry

The nanomechanical model described above offers a testable prediction of the length threshold above which CNTs will mechanically activate this lysosomal damage pathway. The proposed mechanism requires a tube length greater than the lysosome diameter to force the tips in contact with the inner leaflet by compression forces exerted by the confining membrane, together with sufficient stiffness to resist tube buckling. In contrast, short or flexible nanotubes cannot be mechanically forced into contact with the membrane, and should contact the membrane only through Brownian motion or under the influence of electrostatic colloidal forces. Because the samples studied here all have negative surface charge in cell culture medium (*SI Appendix*, Table S3), those electrostatic forces are repulsive and we would not expect persistent tip–membrane contact or lysosomal damage to occur without the mechanical forces associated with the confinement of long, stiff 1D structures. We undertook to test these predictions and validate the model through additional experiments on shortened nanotubes, small-diameter (flexible) nanotubes, and carbon nanohorns (*SI Appendix*, Table S3).

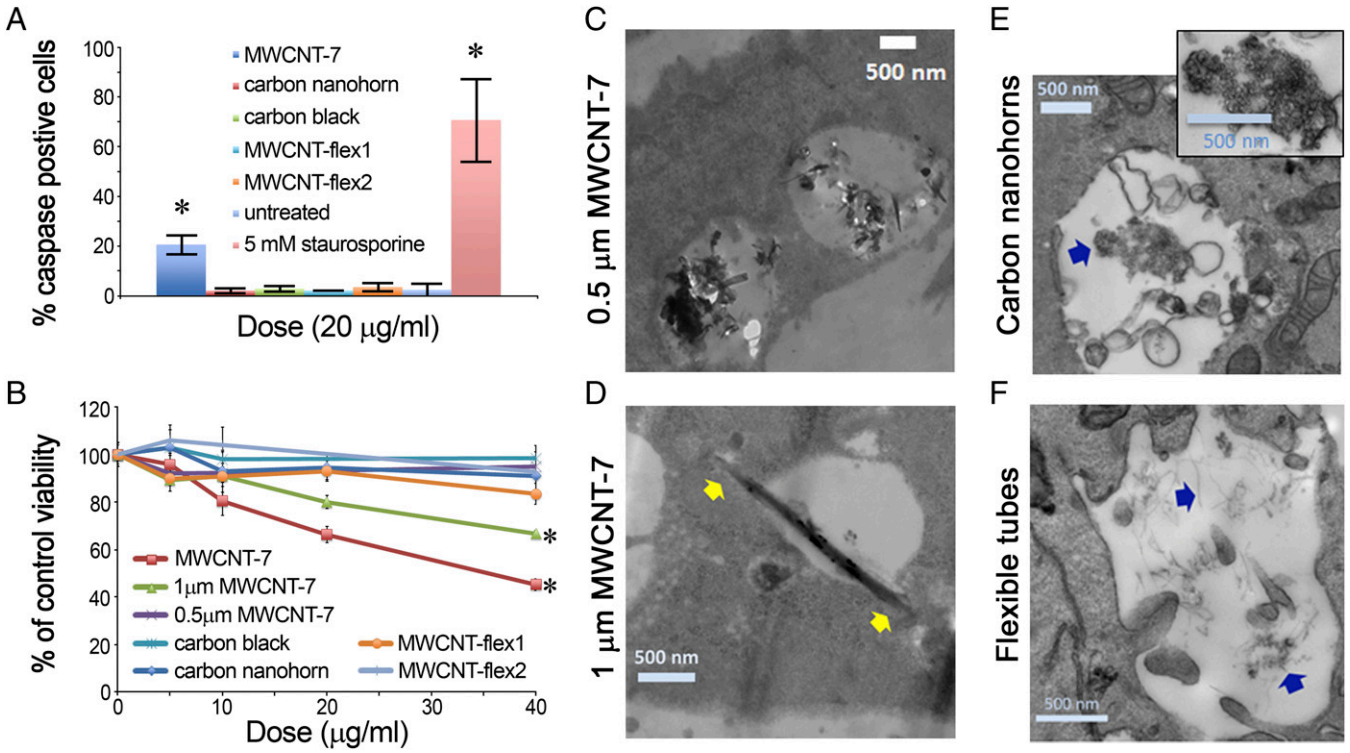

Fig. 4. Cellular interactions with other carbon nanoforms of diverse geometry. (*A*) Quantification of caspase activation 24 h after exposure to carbon nanoparticles. Caspase activation was assessed using sulforhodamine-labeled caspase after exposure of hepatocytes to 20 μg/mL carbon nanomaterials for 24 h or to 5 μM staurosporine for 3 h as positive control. MWCNT-7 significantly (*$P < 0.05$) induced caspase activation. (*B*) Cell viability assessed using the dehydrogenase activity assay WST-8 24 h following exposure to carbon nanomaterials. Flexible MWCNTs, carbon black, and carbon nanohorns did not significantly decrease viability whereas long, rigid MWCNT-7 or 1-μm MWCNT-7 significantly induced toxicity (*$P < 0.05$). (*C–F*) Uptake and localization of various carbon nanoforms in hepatocytes at 24 h after exposure to 10 μg/mL of various carbon nanoforms: (*C*) shortened MWCNT-7 sample, 0.5-μm MWCNT-7; (*D*) 1-μm MWCNT-7; (*E*) isometric carbon nanohorn aggregates; (*F*) thin (flexible) CNTs. Note that carbon nanohorns, flexible CNTs, and 0.5-μm-long MWCNTs are localized in cytoplasmic vesicles, whereas 1-μm-long MWCNTs are seen penetrating through the lysosomal membrane (*D*, yellow arrows).

Uptake and Lysosomal Interactions of Shortened CNTs

The MWCNT-7 sample was progressively shortened using oxidative treatment and ultrasonication followed by thermal annealing to restore the original graphenic surfaces (*SI Appendix*, Table S3 and section 17). The original MWCNT-7 sample (mean length 11.7 μm) induced cathepsin B release (Fig. 3 *D* and *G* and *SI Appendix*, Fig. S31*B*), while the same sample shortened to 0.5 μm was successfully compartmentalized in cytoplasmic vesicles (Fig. 4*C*) and did not induce cathepsin B release from hepatocytes (Fig. 3*G*) or toxicity (Fig. 4*B*). MWCNTs longer than ∼1 μm were observed in contact with, or piercing membranes of cytoplasmic vesicles (Fig. 4*D*) and this sample induced intermediate toxicity (Fig. 4*B* and *SI Appendix*, Fig. S25). The MWCNT length threshold for the onset of toxicity (0.5–1 μm) is in the range of the measured mean lysosome diameter of ∼0.6–1 μm (*SI Appendix*, Fig. S31), which is in agreement with the predictions of the model.

Uptake and Lysosomal Interactions of Carbon Nanohorns and Flexible CNTs

We next investigated whether thin (more flexible) MWCNTs could initiate lysosomal membrane permeabilization and cathepsin B release into the cytoplasm. Two samples of thinner MWCNTs, MWCNT-flex1 and MWCNT-flex2 (*SI Appendix*, Table S3), were compartmentalized into cytoplasmic vesicles in hepatocytes and did not induce cathepsin B release (Figs. 3 *G* and 4*F* and *SI Appendix*, Fig. S27 *H* and *I*). Finally, nanomaterials with ultrasharp features have been reported to pierce lysosomal membranes (9). To investigate the role of ultrafine-scale surface roughness in this sample set, hepatocytes were also exposed to carbon nanohorns, which do not have an overall 1D geometry, but rather are aggregated single-walled nanotube cones with outward protruding high-curvature tips (∼1–3 nm). Agglomerates of carbon nanohorns were observed compartmentalized in cytoplasmic vesicles (Fig. 4*E*) with no release of cathepsin B (*SI Appendix*, Fig. S27*G*). Both the carbon nanohorns and the thinner CNTs have higher surface area than the long, rigid MWCNTs or the carbon black nanoparticles; however, they did not induce cell death at equivalent mass (Fig. 4*B*) or surface area doses (*SI Appendix*, Fig. S25) after 24 or 48 h. Lysosomal damage in this system is not related to high surface area or sharp nanoscale surface features, but rather to length and stiffness.

Pathogenicity Classification Diagram for 1D Nanocarbons

Our combined results can be used to propose a general criterion for the ability of a carbon nanomaterial to induce lysosomal damage by this nanomechanical mechanism. For sustained contact with the lysosome membrane, the encapsulated fibrous material must be able to withstand the confining compressive force without buckling. We thus derived a buckling criterion using the classical Euler theory, where the concentric tubes of an MWCNT are modeled as an equivalent continuum hollow cylinder (*SI Appendix*, Fig. S17). The criterion for buckling relies only on the tube length L and effective diameter d (see details in *SI Appendix*, section 16). Fig. 5 presents the criterion in the form of a classification diagram, where the thick blue curve is the calculated threshold for CNT buckling under a typical compressive force exerted by the lysosomal membrane (20 pN). This buckling curve together with the characteristic lysosome size divides a general set of nanotubes into two categories: "biologically stiff" or "biologically soft." Nanotubes falling in the pink shaded region are predicted to have sufficient stiffness and length to mechanically induce lysosomal permeability leading to cathepsin B release as well as inflammasome activation (17). This nanomechanical theory is compared with data from the present study (square symbols) and the literature (diamonds) in Fig. 5. The red symbols represent samples reported to activate this pathway, and blue symbols represent samples reported to be inactive. The theory correctly identifies pathogenic from nonpathogenic nanocarbons in the broad sample set, although more data will eventually be required to assess the accuracy of the buckling criterion in the borderline region. Note that this theory is for carbons with as-produced graphenic surfaces, and not for functionalized materials, which may involve a wide range of

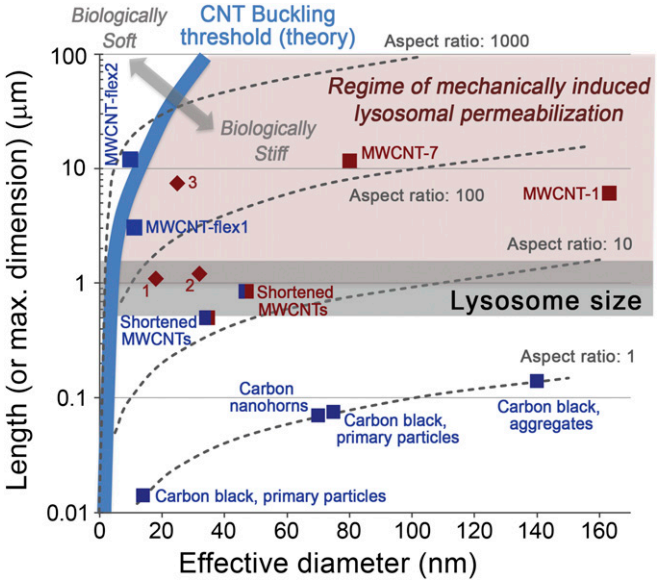

Fig. 5. Generalized classification diagram distinguishing pathogenic from biocompatible carbon nanomaterials in the mechanical pathway to lysosomal membrane damage. The classification diagram is based on the geometric criteria for unfunctionalized carbon nanomaterials to induce lysosomal permeability through mechanical stress. The nanomechanical theory of intracellular buckling (blue curve) is compared with data from the present study (square symbols) and the literature (diamonds). (See *SI Appendix*, Figs. S19, S27, and S29 for MWCNT-1 data.) Red (but not blue) symbols represent samples reported to activate this pathway. Data points labeled 1,2 are literature reports of statistically significant IL-1β release for THP-1 cells at 50 μg/mL MWCNT exposure (17); point 3 is statistically significant IL1-β activity in THP-1 cells above 25 μg/mL exposure to as-produced BSA-coated MWCNTs (10). Also shown are dashed lines of constant AR, which show that nanotubes with intermediate but not low or high AR, together with long length, are the most likely to induce lysosomal damage by mechanical stress.

grafted or adsorbed molecular segments that can interact in chemically specific ways with biological membranes.

High aspect ratio is often cited as a key fiber property associated with pathogenicity. To better understand the role of aspect ratio (AR), Fig. 5 includes dashed lines of constant AR from 1 to 1,000. Isometric nanomaterials (AR∼1) cannot reach the critical lysosome size while remaining at the nanoscale, and are nonpathogenic by this pathway. In contrast, nanomaterials with AR>∼10, and especially AR∼100 often fall in the pathogenic regime. Interestingly, many materials with very high AR (∼>1,000) are also nonpathogenic, as they are too easily buckled to behave as rigid fibers within the lysosome. Buckling is favored by a combination of long length and small diameter (i.e., high AR), and the high AR is therefore unreliable as a simple, monotonic indictor of the potential of a fibrous material to induce pathology.

Our proposed classification diagram can be readily generalized to other 1D materials by choosing an appropriate material-dependent elastic modulus to use in the Euler buckling theory (*SI Appendix*, Fig. S18). For a wide variety of other 1D material classes (metal, oxide, polymer) this generalized classification diagram shows a critical threshold in length/width space that represents a transition from biologically soft to stiff, and thus identifies the important subset of all 1D materials with the potential to induce lysosomal permeability by this nanomechanical mechanism. As an example, the diagram correctly predicts that many thin nanofibrous materials of intrinsic low stiffness [e.g., polymers, worm-like micelles (32)] would be nonpathogenic by this pathway.

Conclusions

The confinement of 1D nanomaterials in intracellular lipid-bilayer vesicles produces conformations and behaviors that are revealed

by MD and in vitro bioimaging. Cellular attempts to package long 1D nanomaterials in spherical vesicles leads to material compression that forces persistent mechanical contact between the tube tip and inner membrane leaflet, which for CNTs causes lipid extraction, membrane permeabilization, release of cathepsin B, and cell death by apoptosis. In contrast, this mechanism predicts intact lysosomes and lower toxicity for nanotubes that are short (<~1 μm), or of very high L/D that easily buckle in the presence of the lysosomal compression force (~20 pN), or for other materials with similar graphenic chemistry but isometric shape (e.g., carbon black, carbon nanohorns). These predictions are validated by in vitro experiments using hepatocytes as well as lung epithelial cells exposed to a diverse panel of synthetic nanocarbons. A quantitative material classification diagram distinguishes pathogenic from biocompatible nanotube varieties based on a buckling criterion that relies only on minimum and maximum dimension. The present results also suggest that the observed low pathogenicity of tangled tubes relative to straight tubes (3, 21) may be usefully understood as an effect of intrinsic biological softness, defined as the resistance to buckling under lysosomal compressive forces. Unlike tangling, which is an agglomeration or deformation state subject to change through material handling or processing, biological softness is a fundamental nanomaterial property directly related to diameter and length. This mechanistic understanding provides guidance for safe design and material selection of 1D nanomaterials for both biomedical and nonbiomedical applications.

Methods

CGMD Simulations. CGMD simulations of a CNT encapsulated inside a lysosome were performed to investigate the maximum noninterrupted contact time between the CNT and a membrane patch built from solvent-free CG lipids (4, 22). Further details of the CG models of the membrane and CNT can be found in *SI Appendix*, sections 2 and 3.

All-Atom MD Simulations. All-atom MD simulations were performed to investigate how an MLG, corresponding to a near-tip slice of an MWCNT, or an MWCNT interacts with a membrane patch. The membranes were constructed from bilayers of the Berger lipids. The Berger lipid force field was used for lipids combined with an Optimized Potentials for Liquid Simulations representation of MLGs and MWCNTs. DPPC was adopted to build the lipid bilayer. Further details are provided in *SI Appendix*, section 9.

Nanomaterial Panel and Characterization. A panel of carbon nanomaterials of diverse geometry and stiffness was assembled and characterized, including commercial MWCNTs from Mitsui & Co. (MWCNT-7) and NanoLab, Inc., which were synthesized using catalytic chemical vapor deposition. The process of shortening and surface restoration used to create variants of the MWCNT-7 sample is described in *SI Appendix*, section 17. The panel of carbon nanomaterials included zero-dimensional reference materials including carbon black M120 (Cabot Corporation) and carbon nanohorns, courtesy of David Geohegan, Oak Ridge National Laboratory, Oak Ridge, TN, as isometric (low-AR) reference carbon materials.

Cell Culture and Exposure Conditions. Experiments were conducted on two cell types: hepatocytes (AML12 cells; American Type Culture Collection; CRL-2254) and lung epithelial cells (H460 cells; American Type Culture Collection; HTB-177). The cells were exposed to commercial MWCNTs, carbon nanohorns, and carbon black and assessed for viability as described in *SI Appendix*, Figs. S19 and S20.

Lysosomal Permeabilization. After exposure of cells to carbon nanomaterials, the integrity of lysosomes is determined using a cathepsin B target peptide sequence conjugated to a red fluorophore, which is cleaved by active cathepsin B enzyme. Diffuse red cytoplasmic fluorescence indicates lysosomal membrane permeabilization whereas punctate cytoplasmic fluorescence indicates intact lysosomes. Lysosomal permeabilization was quantified using cell segmentation and analysis and quantitative high content fluorescence imaging as described in *SI Appendix*, section 17.

ACKNOWLEDGMENTS. The authors acknowledge a generous gift from Donna McGraw Weiss and Jason Weiss. This work was supported by the National Science Foundation (Grants CBET-1344097 and CMMI-1562904) and the Superfund Research Program of the National Institute of Environmental Health Sciences (Grant P42 ES013660). The simulations reported were performed on resources provided by the Extreme Science and Engineering Discovery Environment (XSEDE) through Grant MS090046.

1. Tu Y, et al. (2013) Destructive extraction of phospholipids from Escherichia coli membranes by graphene nanosheets. *Nat Nanotechnol* 8(8):594–601.
2. Li Y, et al. (2013) Graphene microsheets enter cells through spontaneous membrane penetration at edge asperities and corner sites. *Proc Natl Acad Sci USA* 110(30):12295–12300.
3. Nagai H, Toyokuni S (2012) Differences and similarities between carbon nanotubes and asbestos fibers during mesothelial carcinogenesis: Shedding light on fiber entry mechanism. *Cancer Sci* 103(8):1378–1390.
4. Shi X, von dem Bussche A, Hurt RH, Kane AB, Gao H (2011) Cell entry of one-dimensional nanomaterials occurs by tip recognition and rotation. *Nat Nanotechnol* 6(11):714–719.
5. Vecitis CD, Zodrow KR, Kang S, Elimelech M (2010) Electronic-structure-dependent bacterial cytotoxicity of single-walled carbon nanotubes. *ACS Nano* 4(9):5471–5479.
6. Zhang S, Li J, Lykotrafitis G, Bao G, Suresh S (2009) Size-dependent endocytosis of nanoparticles. *Adv Mater* 21(4):419–424.
7. Li R, et al. (2013) Surface charge and cellular processing of covalently functionalized multiwall carbon nanotubes determine pulmonary toxicity. *ACS Nano* 7(3):2352–2368.
8. Stern ST, Adiseshaiah PP, Crist RM (2012) Autophagy and lysosomal dysfunction as emerging mechanisms of nanomaterial toxicity. *Part Fibre Toxicol* 9(1):20.
9. Chu Z, et al. (2014) Unambiguous observation of shape effects on cellular fate of nanoparticles. *Sci Rep* 4:4495.
10. Wang X, et al. (2012) Pluronic F108 coating decreases the lung fibrosis potential of multiwall carbon nanotubes by reducing lysosomal injury. *Nano Lett* 12(6):3050–3061.
11. Elbaum M, Kuchnir Fygenson D, Libchaber A (1996) Buckling microtubules in vesicles. *Phys Rev Lett* 76(21):4078–4081.
12. Fygenson DK, Elbaum M, Shraiman B, Libchaber A (1997) Microtubules and vesicles under controlled tension. *Phys Rev E Stat Phys Plasmas Fluids Relat Interdiscip Topics* 55(1):850–859.
13. Donaldson K, et al. (2013) Pulmonary toxicity of carbon nanotubes and asbestos - similarities and differences. *Adv Drug Deliv Rev* 65(15):2078–2086.
14. Hamilton RF, et al. (2009) Particle length-dependent titanium dioxide nanomaterials toxicity and bioactivity. *Part Fibre Toxicol* 6:35.
15. Bussy C, et al. (2012) Critical role of surface chemical modifications induced by length shortening on multi-walled carbon nanotubes-induced toxicity. *Part Fibre Toxicol* 9(1):46.
16. Wang X, et al. (2011) Dispersal state of multiwalled carbon nanotubes elicits profibrogenic cellular responses that correlate with fibrogenesis biomarkers and fibrosis in the murine lung. *ACS Nano* 5(12):9772–9787.
17. Hamilton RF, Jr, Wu Z, Mitra S, Shaw PK, Holian A (2013) Effect of MWCNT size, carboxylation, and purification on in vitro and in vivo toxicity, inflammation and lung pathology. *Part Fibre Toxicol* 10(1):57.
18. Yang M, et al. (2013) Functionalization of carbon nanoparticles modulates inflammatory cell recruitment and NLRP3 inflammasome activation. *Small* 9(24):4194–4206.
19. Kraszewski S, Bianco A, Tarek M, Ramseyer C (2012) Insertion of short amino-functionalized single-walled carbon nanotubes into phospholipid bilayer occurs by passive diffusion. *PLoS One* 7(7):e40703.
20. Lacerda L, et al. (2013) How do functionalized carbon nanotubes land on, bind to and pierce through model and plasma membranes. *Nanoscale* 5(21):10242–10250.
21. Poland CA, et al. (2008) Carbon nanotubes introduced into the abdominal cavity of mice show asbestos-like pathogenicity in a pilot study. *Nat Nanotechnol* 3(7):423–428.
22. Reynwar BJ, et al. (2007) Aggregation and vesiculation of membrane proteins by curvature-mediated interactions. *Nature* 447(7143):461–464.
23. Keten S, Xu Z, Ihle B, Buehler MJ (2010) Nanoconfinement controls stiffness, strength and mechanical toughness of β-sheet crystals in silk. *Nat Mater* 9(4):359–367.
24. Hategan A, Law R, Kahn S, Discher DE (2003) Adhesively-tensed cell membranes: lysis kinetics and atomic force microscopy probing. *Biophys J* 85(4):2746–2759.
25. Kühnel W (2003) *Color Atlas of Cytology, Histology, and Microscopic Anatomy* (Thieme, New York), 4th Ed, p 34.
26. Lee HJ, Peterson EL, Phillips R, Klug WS, Wiggins PA (2008) Membrane shape as a reporter for applied forces. *Proc Natl Acad Sci USA* 105(49):19253–19257.
27. Bell GI (1978) Models for the specific adhesion of cells to cells. *Science* 200(4342):618–627.
28. Ji Z, et al. (2009) The hepatotoxicity of multi-walled carbon nanotubes in mice. *Nanotechnology* 20(44):445101.
29. Kettiger H, Schipanski A, Wick P, Huwyler J (2013) Engineered nanomaterial uptake and tissue distribution: From cell to organism. *Int J Nanomedicine* 8:3255–3269.
30. Jordans S, et al. (2009) Monitoring compartment-specific substrate cleavage by cathepsins B, K, L, and S at physiological pH and redox conditions. *BMC Biochem* 10(1):23.
31. Reiners JJ, Jr, et al. (2002) Release of cytochrome c and activation of pro-caspase-9 following lysosomal photodamage involves Bid cleavage. *Cell Death Differ* 9(9):934–944.
32. Geng Y, et al. (2007) Shape effects of filaments versus spherical particles in flow and drug delivery. *Nat Nanotechnol* 2(4):249–255.